The effect of thermal post-processing treatment on laser powder bed fusion processed NiMnSn-based alloy for magnetic refrigeration

Sun, Kun; Li, Sheng; Mohamed, Abd El-Moez A.; Ma, Kan; Duan, Ranxi; Brooks, Oliver Peter; Jeong, Minki; Head, Jake; Sheridan, Richard S.; Attallah, Moataz M.

DOI:
10.1016/j.jallcom.2023.171063

Journal of Alloys and Compounds 961 (2023) 171063

Contents lists available at ScienceDirect

Journal of Alloys and Compounds

journal homepage: www.elsevier.com/locate/jalcom

The effect of thermal post-processing treatment on laser powder bed fusion processed NiMnSn-based alloy for magnetic refrigeration

Kun Sun [a], Sheng Li [b], Abd El-Moez A. Mohamed [a], Kan Ma [a], Ranxi Duan [a], Oliver Peter Brooks [a], Minki Jeong [c], Jake Head [c], Richard S. Sheridan [a], Moataz M. Attallah [a,*]

[a] School of Metallurgy and Materials, University of Birmingham, B15 2TT Birmingham, United Kingdom
[b] School of Electro-mechanical Engineering, Guangdong University of Technology, 510006 Guangdong, China
[c] School of Physics and Astronomy, University of Birmingham, B15 2TT Birmingham, United Kingdom

ARTICLE INFO

Article history:
Received 13 March 2023
Received in revised form 6 June 2023
Accepted 19 June 2023
Available online 21 June 2023

Keywords:
Laser powder bed fusion
Heat treatment
Microstructure
Magnetic entropy change
And Magnetocaloric material

ABSTRACT

This study investigates the effects of heat treatment (HT) time (one, two, and three weeks) on the microstructure and magnetocaloric effect (MCE) of laser powder bed fusion (LPBF) NiMnSn alloys. Increasing the HT time improves chemical homogeneity, and decreases the local misorientation imparted by the LPBF process. This is also associated with an enhancement in the maximum magnetic entropy change (ΔS_m) values around the martensitic transformation temperature (T_M), which increases from 0.2 J kg^{-1} K^{-1} to 0.45 J kg^{-1} K^{-1} under 1 T applied magnetic field. However, the ΔS_m of the one-week HTed sample around the curie temperature (T_c) (0.90 J kg^{-1}K^{-1} at 315 K) is slightly lower than the two weeks and three weeks HTed samples (0.99 J kg^{-1}K^{-1} at 320 K, 0.94 J kg^{-1}K^{-1} at 320 K), respectively.

1. Introduction

Compared with traditional cooling technologies, magnetic refrigeration has the advantages of producing lower noise, higher efficiency and being environmentally friendly materials [1]. Several magnetocaloric materials have been investigated for magnetic refrigeration, especially rare-earth-based alloys [2], however, Heusler alloys (HAs) have been reported as the most suitable candidates due to the lower cost, non-toxic properties, and outstanding magnetocaloric effect (MCE) [3,4]. NiMnSn HA is an intermetallic compound with high room temperature MCE and has been investigated in several previous works [5,6]. It has been reported that the nanocrystalline state and HT processes are essential in determining martensite structure and transition temperature in these alloys [7,8]. HT affects the exchange interaction and magnetic properties by modifying the short-range interactions [9]. Dan et al.[10] studied $Ni_{50}Mn_{50-x}Sn_x$ alloys with a wide range of Sn-concentration (x = 0–40), fabricated by arc-melting and subsequent annealing. By changing Sn-concentration, the Martensitic transformation temperature changed from 150 K to 350 K. Thus, improving the composition uniformity is essential for LPBF-fabricated NiMnSn parts, to ensure a consistent working temperature in the magnetic refrigeration field. Ghosha and Mandal [11] prepared a series of $Ni_{50}Mn_{36.5}Sn_{13.5}$ samples with various HTs (annealing 0, 6, 12, 18, and 24 h at 1173 K, followed by ice water quenching) and studied their magnetocaloric properties. Magnetic hysteresis and (the magnetic entropy change) ΔS increased with increasing annealing times, from 0 to 24 h. There have been reports of additional phases observed (Ni_3Sn_2 and $Mn_{1.77}Sn$) in melt-spun ribbons where the cooling rate is in the order of ~10^6 K/s [12]. The Heusler structure ($L2_1$) is energetically the most favourable for formation [13]; however, it is challenging to obtain a homogeneous phase distribution, with up to 5 % of Ni_3Sn_2 detectable within the microstructure [13,14].

In magnetic refrigeration systems, the high surface area of heat exchangers allows higher efficiency of heat transfer. However, increasing the surface area of magnetic refrigerants by traditional methods such as machining has the challenge of cracking due to the low mechanical strength of magnetic materials [15]. Laser powder bed fusion (LPBF) is an effective method for manufacturing heat exchangers with high surface-to-volume ratios without the need for machining and reducing material loss. The higher cooling rates induced in LPBF result in an inhomogeneous microstructure in parts built using in-situ alloyed powder [16], due to local variations in

* Corresponding author.
E-mail address: m.m.attallah@bham.ac.uk (M.M. Attallah).

https://doi.org/10.1016/j.jallcom.2023.171063

Table 1
Information on powder used for in-situ alloying.

Elements	Ni	Mn	Sn
The size range (μm)	20–45	< 44	< 45
The shape of the powder	Spherical	cubic	Spherical
Melting point (°C)	1455	1426	231.9
Boiling point (°C)	2913	2061	2602

chemical composition, which significantly influences the magnetocaloric performance.

In this study, we investigate the influence of post-processing HT on the microstructure, magnetic and MCE properties of LPBF $Ni_{50}Mn_{37}Sn_{13}$ HAs in-situ alloy as a low-cost approach and alternative to the pre-alloyed powder.

2. Experimental

2.1. In-situ powder alloying

To fabricate in-situ $Ni_{50}Mn_{37}Sn_{13}$ (NiMnSn) bulk HAs, Ni, Mn, and Sn elements were blended in stochiometric amounts. The properties of these raw elements are detailed in Table 1. The in-situ powder was mixed for two days in an argon atmosphere to ensure the powder's homogeneity. Fig. 1 presents a schematic of the blending process and powder morphology. Additional 2 at% Mn and 1 at% Sn powder were added to compensate for the evaporation of Mn and Sn elements during the LPBF process.

2.2. LPBF process and post-processing heat treatment

NiMnSn bulk HAs (5 × 5 × 10 mm) were fabricated via the LPBF technique. These bulk samples were manufactured on top of a steel substrate in a controlled argon environment (O_2 < 500 ppm) using a Concept Laser M2 machine with a continuous wave mode Yb-fibre laser (λ = 67 nm, maximum laser power = 400 W) as a primary heat source for melting. A 90°raster scan strategy was used for LPBF NiMnSn bulk samples, as shown in Fig. 2. Table 2 shows the LPBF processing parameters and HT processes used for each of the samples in this study. Three groups of samples were encapsulated in separate quartz tubes filled with argon and individually heat treated at 940 °C (10 °C/min ramping rate) for one, two and three weeks before being quenched into water (see Table 2).

2.3. Microstructural characterisation and magnetic measurements

The microstructure at room temperature was examined using a Hitachi TM3030 scanning electron microscope (SEM). A Quanta 3D FEG SEM with electron backscatter diffraction (EBSD) and Energy-dispersive X-ray Spectroscopy (EDS), was used to analyse the microstructure and crystal orientations (step size of 1.5 μm). The Mn segregation and secondary phases were investigated using a Tecnai F20 transmission electron microscope (TEM) where appropriate, along with high-angle annular dark-field scanning TEM imaging and EDS mapping. The TEM samples were prepared using focus ion beam

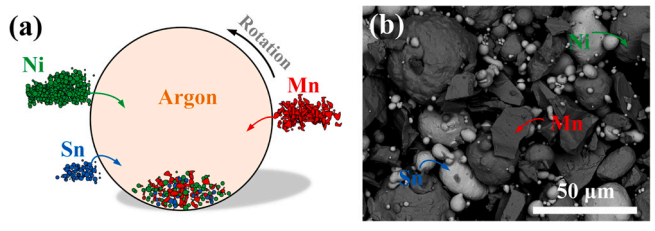

Fig. 1. (a) Schematic of the blending processing and (b) The backscattered electron image of NiMnSn blended powder.

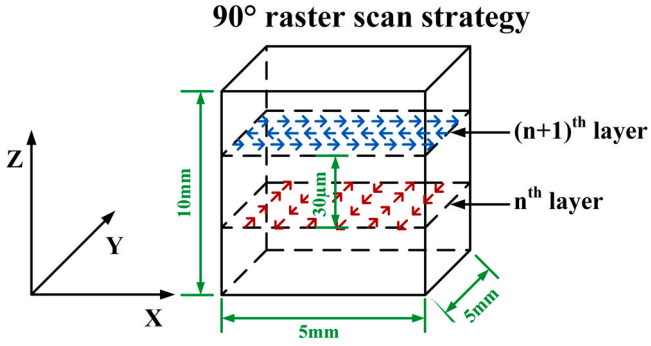

Fig. 2. The scan strategy used for the manufacture of each LPBF sample.

(FEI FIB Quanta 3D SEM) milling. TEM was conducted immediately following the creation of the TEM sample using FIB to prevent oxidation. Magnetic measurements were performed using a superconducting quantum interference device (SQUID) magnetometer magnetic properties measurements system. The temperature-dependent magnetisation curves (M-T curves) were obtained in zero-field cooled warming, field-cooled cooling, and field-cooled warming modes at 0.01 T and 1 T, all of which investigate the magnetic phase transitions and hysteresis. Under applied magnetic fields of up to 1 T, isothermal magnetisation curves were measured every 5 K. The change in magnetic entropy (ΔS) was calculated using Maxwell's relation (Eq. (1)) [1], where H_F: the final magnetic field strength; and H_I: the initial magnetic field strength).

$$\Delta S = \int_{H_I}^{H_F} \left(\frac{\partial M}{\partial T}\right)_H dH \tag{1}$$

3. Results and discussion

3.1. Microstructure

3.1.1. Influence of HT on the microstructure

SEM micrographs for the as-fabricated (AF) and heat-treated (HT) samples are shown in Fig. 3. The micrographs show that the AF sample contains segregations of Sn, Ni and Mn (See Fig. 3a, b), which are diffused in the matrix alloy after HT, enhancing homogeneity. The Ni element is a based alloying element. Mn segregations are observed even after the three weeks' HT process. Fig. 3f and the corresponding EDS map show Mn segregations which contain oxygen elements, which is also proved by the EDS result in Fig. 5.

Fig. 4 shows the XRD patterns with different HT times at room temperature. The AF sample shows the $L2_1$ austenite phase at room temperature. After HT, the three samples display highly ordered cubic $L2_1$ austenite phase, with minor peaks relevant to MnO. Mn is highly sensitive to oxygen, therefore MnO was observed within the structure due to oxygen infiltration during the LPBF process [17].

To confirm the structure of the segregated Mn, the diffraction pattern (Kikuchi pattern) was obtained using EBSD, as shown in Fig. 5. The red cross shows the Kikuchi pattern (Fig. 5b) and d)) from the $L2_1$ Ni_2MnSn structure, which is the primary phase. The Kikuchi pattern also confirmed the MnO cubic phase within the regions of Mn segregation. The EDS line analysis result was obtained through the Mn segregation, as shown in the inset picture in Fig. 5a). The O and Mn elements increased significantly, especially the Mn, whereas the Ni and Sn concentrations have significantly decreased in this region. The EDS compositional analysis shows that the small area of Mn segregation contains 1.7 at% Ni, 84.3 at% Mn, 1.4 at% Sn, and 12.6 at% O elements, as shown in the inset table in Fig. 5a).

Table 3 and Fig. 6 illustrate the chemical composition, morphology, and distribution of secondary phases within the No. 3

Table 2
The LPBF processing parameters and HT processes.

No.	Laser Power (W)	Scan Speed (mm/s)	Thickness (mm)	Scan spacing (mm)	The volume Energy density (J/mm^3)	The heat treatment process
AF	125	1750	0.03	0.05	47.62	/
No.1						940 °C-one week-Quench
No.2						940 °C-two weeks-Quench
No.3						940 °C-three weeks-Quench

sample using TEM. The Mn-rich phases (dark grey phase in Fig. 6a)–c)) can be seen clearly. The selected area electron diffraction (SAED) in the 1st red dotted circle and the EDS at point **a** further show the Mn-rich phase contains MnO. The NiSn-rich phases (white phases) in the Mn-rich region (see Fig. 6a)) are $L2_1$-type Ni_2MnSn phases, as proven by the SAED in the 2nd red dotted circle and the EDS at point **b**. The crystal structure of the matrix is also the $L2_1$-type phase (see the SAED in the 3rd red dotted circle **c**, as shown in Fig. 6e)). However, the chemical composition of the matrix differs from the white phases, as shown in Table 3. The EDS at point **d** with high Mn at% proved the appearance of Mn segregation. MnO is a face-centred cubic antiferromagnetic phase [18] which has been shown to have deleterious effects on the MCE of these alloys [19].

As shown in the SEM pictures in Fig. 7, the Mn segregation is observed within all samples, proving that the HT process can not dissolve the Mn segregations. All grains within LPBF samples are equiaxed. Fig. 7 also shows the inverse pole figure (IPF) images of the AF and HT samples. The different colours within IPF images represent the different orientations of the unit cells across the grains. As shown in Fig. 7c, g, k, and o, all samples exhibited various colours, demonstrating how the samples did not possess strong preferential orientations.

A kernel-averaged misorientation (KAM) map estimates the plastic strain in individual grains, revealing local variations in lattice orientations and suggesting the change of dislocation density in the material [20,21]. Fig. 7d, h, l, and p present KAM maps of the LPBF NiMnSn alloys in AF and HT conditions. Higher local misorientation was observed in the AF sample (Fig. 7d), with an average KAM value of 0.34. Due to the complex thermal cycling, the rapid heating and solidification cycles in the LPBF process, plastic strain and residual stresses are created in the AF samples, which induced a higher dislocation density [22,23]. In contrast, the KAM map of the No.1 sample presents a slight decrease in misorientation. The average KAM value decreased to 0.31. When the annealing time increased to two and three weeks, the average local misorientation within samples was further reduced to 0.21 and 0.23 respectively, indicating the internal plastic strain is relieved [21]. The local misorientation within the LPBF samples decreased with increasing HT time as the rate of atomic diffusion increased and atoms preferred to move from high- to low-stress regions at high temperatures (940 °C) [23]. The KAM is often used as a qualitative measure of localised plastic deformation [24,25]. Strain can indirectly represent residual stresses [26]. The HT processes (two weeks and three weeks) remove local misorientation (see Fig. 7) and therefore, can release some stored strain and residual stresses imparted by the LPBF process.

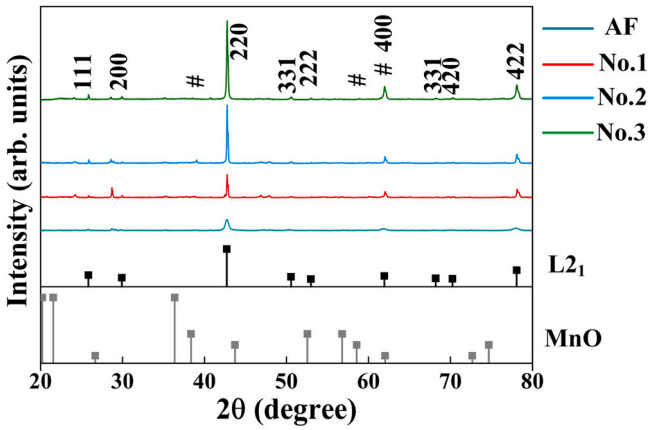

Fig. 4. XRD patterns of annealed LPBF NiMnSn alloys. The # peaks fit the MnO phase. Other peaks correspond to the $L2_1$ Heusler phase.

3.1.2. Composition evolution

The composition evolution also plays a vital role in the magnetic properties, as the ratio of the three elements affects the characteristic transformation temperatures and the MCE [10,27,28]. To investigate the evolution of the chemical composition upon the HT time NiMnSn alloys, SEM-EDS was used. Five random small areas without Mn segregations within three different random areas of each sample (the total amount is 15 small areas) were selected for the SEM-EDS test. The composition for each sample is defined as: Ni_{Ci}, Mn_{Ci}, and Sn_{Ci} (i is from 1 to 15). Ni_{C0}, Mn_{C0}, and Sn_{C0} are the average chemical composition. The composition deviation of Ni, Mn, and Sn elements (ζ_{Ni}, ζ_{Mn}, and ζ_{Sn}) is introduced and calculated regarding Eqs. (2)–(4) [29]. The composition deviation of oxygen

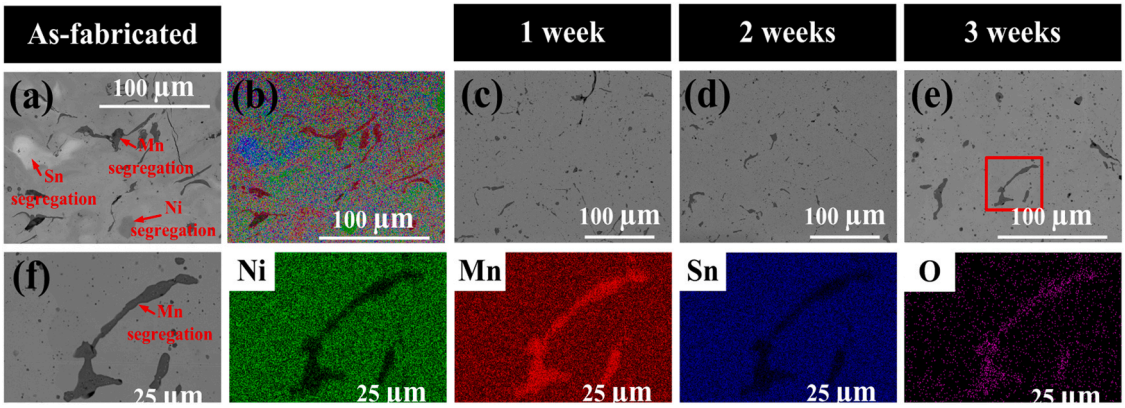

Fig. 3. SEM-BSE micrographs of the microstructure of (a) the as-fabricated sample; (b) the Mixed EDS map for the as-fabricated sample; (c, d, e) the HT samples; (e) and (f) the Mn segregation (red box in (e)).

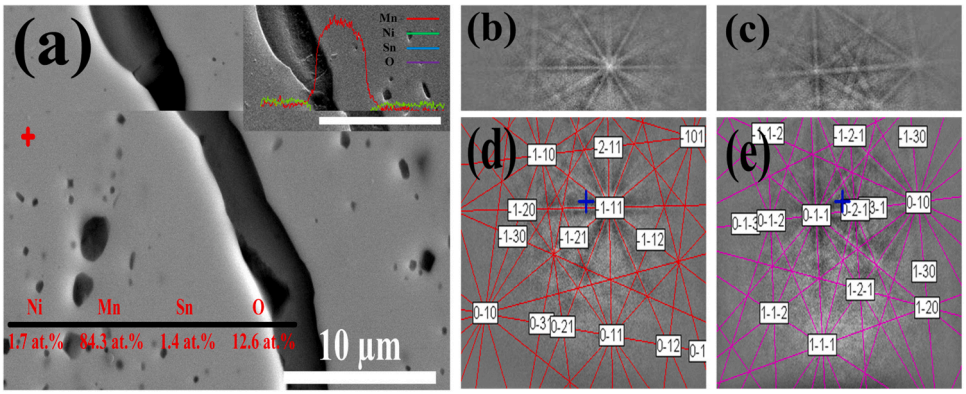

Fig. 5. (a) The SEM picture of the No.3 sample (the inset picture is the EDS line analysis); (b and d) the EBSD Kikuchi pattern from $L2_1$ Ni_2MnSn structure in the No.3 sample; and (c and e) the EBSD Kikuchi pattern from MnO structure in the No.3 sample.

Table 3
The EDS result of four points in Fig. 6.

	Ni (at%)	Mn (at%)	Sn (at%)	O (at%)
a	0.3	49.2	0.2	50.4
b	45.3	23.5	29.1	2.2
c	51.7	28.9	18.3	1.2
d	0.8	94.0	0.4	4.8

should not be calculated as it always combines with the Mn segregation. The composition deviation (ζ) for all components in a sample is calculated regarding Eqs. (2)–(5).

$$\zeta_{Ni} = [(Ni_{C1} - Ni_{C0})^2 + (Ni_{C2} - Ni_{C0})^2 + \ldots + (Ni_{C15} - Ni_{C0})^2]/15 \quad (2)$$

$$\zeta_{Mn} = [(Mn_{C1} - Mn_{C0})^2 + (Mn_{C2} - Mn_{C0})^2 + \ldots + (Mn_{C15} - Mn_{C0})^2]/15 \quad (3)$$

$$\zeta_{Sn} = [(Sn_{C1} - Sn_{C0})^2 + (Sn_{C2} - Sn_{C0})^2 + \ldots + (Sn_{C15} - Sn_{C0})^2]/15 \quad (4)$$

$$\zeta = \zeta_{Ni} + \zeta_{Mn} + \zeta_{Sn} \quad (5)$$

As shown in Table 4, although the different HT processes did not have a great effect on the average chemical composition, the overall compositional deviation was reduced. The compositional deviation (ζ) decreased from 0.413 to 0.339 with increasing HT time from one week to three weeks, which means the chemical composition

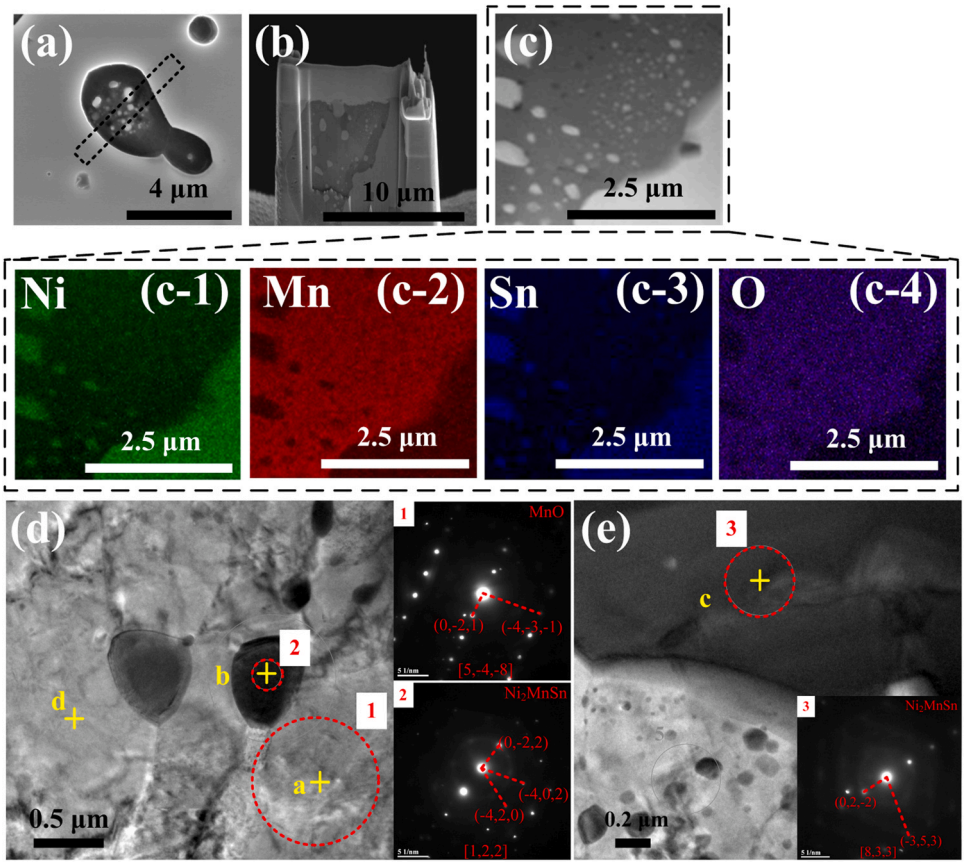

Fig. 6. The SEM micrograph of (a) the FIB lift-out region with Mn segregation in the No.3 sample; (b) TEM samples; (c) STEM bright-field image showing the precipitate-matrix boundary and nano-scale phases within the precipitates with corresponding element mapping by STEMEDS; and (d and e) The TEM image and SAED pattern were collected from the red dotted circle.

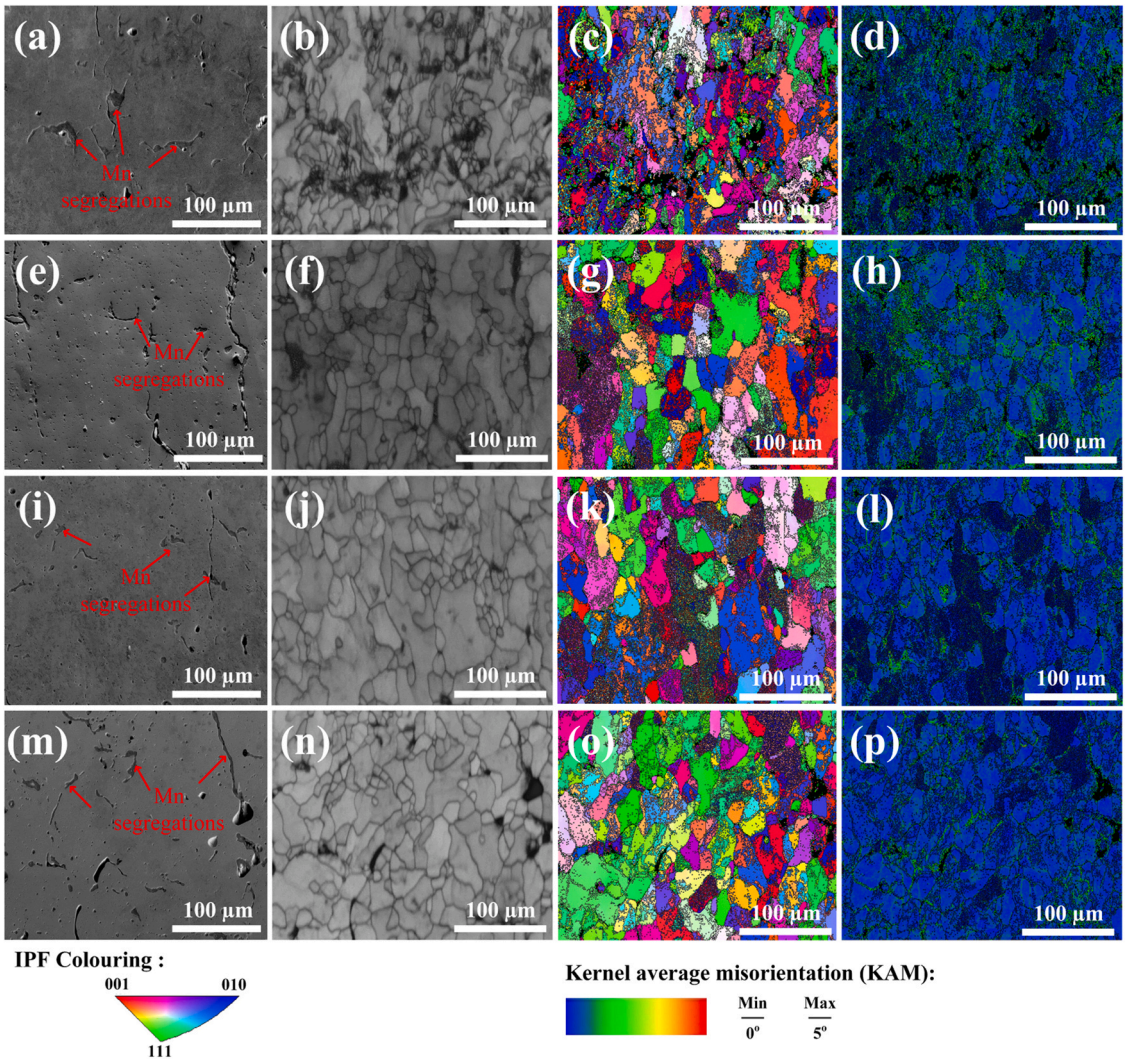

Fig. 7. EBSD analysis of the AF and HT NiMnSn alloy (X-Z section) (the SEM picture, corresponding image quality maps, IPF map, and KAM map): (a-d) as-fabricated sample; (e-h) annealed for one week; (i-l) annealed for two weeks; and (m–p) annealed for three weeks.

becomes more uniform. The ζ_{Mn} and ζ_{Sn} decreased from 0.175 and 0.161–0.062 and 0.023, respectively, when the HT time increased from one week to three weeks, as the long HT time improved the diffusion of Mn and Sn through the structure. The O and corresponding Mn elements were deleted to obtain the accurate chemical composition of the matrix and the valence electron concentration (e/a), as O always combines with Mn to produce MnO, as shown in Figs. 3 and 4. As shown in Table 4, the e/a of the No.1 sample was the biggest (8.038), then it decreased to 8.025 and 8.029 for No.2 and No.3, respectively, which affects the characteristic temperature of structural transition (as shown in Fig. 9 and Table 5) as FOPT is sensitive to chemical composition changes [27,30].

3.2. Magnetic properties

3.2.1. Thermo-magnetisation curve

Fig. 8a shows the thermo-magnetisation curve in an applied field of 0.01 T, with Fig. 8b showing dM/dT vs Temperature for the HT NiMnSn alloys. The AF sample's magnetisation does not show the structural transformation. In contrast, the HT samples show a different behaviour, where the magnetisation remains constant with the increase in temperature up to 30 K (T^*), as the spin moments are locked/frozen [21,24]. The further increase in temperature above T^* increases the thermal energy of these spin moments, leading to unlocking and observing an abrupt increase in magnetisation [21]. The HT samples show two transitions in an applied field of 0.01 T., the martensite-austenite structural transition occurs at 150 K, and the ferromagnetic to paramagnetic transition occurs at the Curie temperature (T_c~320 K, see Table 5). The AF sample does not show any transition. The chemical composition is more uniform after long

Table 4
The average chemical composition and the composition deviation for LPBF samples with different HT processes.

Sample	Average Composition	Average Composition without MnO	ζ	ζ_{Ni}	ζ_{Mn}	ζ_{Sn}	e/a
No.1	$Ni_{48.0}Mn_{32.9}Sn_{15.7}O_{3.4}$	$Ni_{51.5}Mn_{31.6}Sn_{16.9}$	0.413	0.078	0.175	0.161	8.038
No.2	$Ni_{48.1}Mn_{32.5}Sn_{16.1}O_{3.2}$	$Ni_{51.5}Mn_{31.3}Sn_{17.1}$	0.343	0.178	0.130	0.035	8.025
No.3	$Ni_{47.8}Mn_{33.5}Sn_{15.6}O_{3.0}$	$Ni_{50.9}Mn_{32.5}Sn_{16.6}$	0.339	0.254	0.062	0.023	8.029

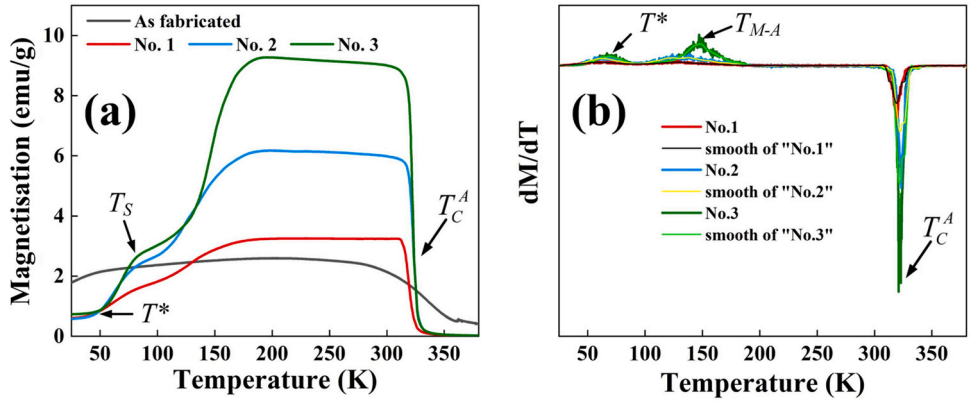

Fig. 8. (a) Thermo-magnetisation curves in an applied field of 0.01 T for the HT NiMnSn alloys; (b) the dM/dT vs temperature for NiMnSn alloys.

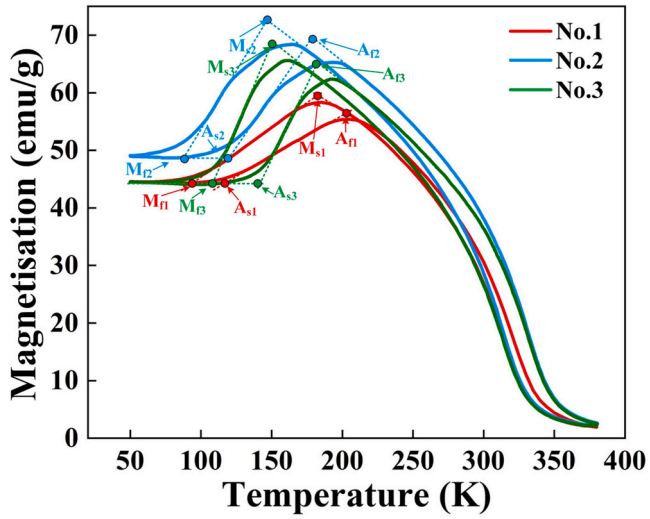

Fig. 9. Thermo-magnetisation curves in an applied field of 1 T for the annealed LPBF processed NiMnSn alloys.

Table 5
The characteristic temperature of the magnetic phase transformation.

Sample	M_s (K)	M_f (K)	A_s (K)	A_f (K)	T_c (K)	T_M (K)
No. 1	182	94	117	203	319.2	149
No. 2	146	89	118	177	322.1	132.5
No. 3	150	108	140	181	322.6	144.8

HT processes, as shown in Table 5. Therefore, uniform chemical composition and homogeneity are more important factors affecting the magnetic properties of LPBF NiMnSn alloys. The long HT process releases stress in the structure, re-ordering the Mn-Mn distance and enhancing the magnetisation [7,31,32]. Thus, the sample with the longest HT processing time (No. 3) has a more uniform chemical composition, homogeneity and reduced stress, leading to more significant magnetisation. The T_c of the samples are deduced from the dM/dT vs Temperature curve in Fig. 8b, which proves that the variation in chemical composition and homogeneity has minimal effect on the T_c. In addition, there is no evidence of the Néel temperature for MnO, as there was only a trace MnO present in these samples. This antiferromagnetic transition of MnO occurs around 120 K and shows only a slight kink in pure MnO, which is not apparent from these magnetisation measurements [33].

3.2.2. Temperature dependence of magnetisation at 1 T magnetic field

As shown in Fig. 9, the field cooling (FC) and field warming (FW) curves measured at 1 T were used to study the characteristics of the magnetic phase transformations. The FC and FW curves provided further evidence of the structural transformation in the annealed samples [34–36]. Thus, the transition around T_M might be the weak first-order structural transformation (FOPT) [37]. The characteristic transformation temperatures for the structural transformation (austenitic start temperature (A_s), austenitic finish temperature (A_f), martensite start temperature (M_s), and martensite finish temperature (M_f)), as well as the thermal hysteresis (ΔT_{hys}), are essential. These temperatures were calculated by extrapolating from both sides of bends in curves through intersections between straight lines [34,35]. The martensitic transformation temperature (T_M) is determined as $((A_s + A_f + M_s + M_f)/4)$. The thermal hysteresis between the FC and FW curves was defined as the difference between A_s and M_f ($\Delta T_{hys} = A_s - M_f$) [34,35], confirming the nature of the martensite transition [31]. Table 5 shows the structural characteristic transformation temperatures at 1 T and T_c at 0.01 T. With decreasing temperature from the M_s, the martensite phase increased, and the austenite phase decreased. The magnetisation decreased down to M_f, where all austenite phases transform into the martensite phase as the austenite phase possesses higher magnetisation than martensite [30]. When increasing the temperature from the A_s, the martensite phase transforms into austenite, and the magnetisation gradually increases until it reaches A_f. Here, all the martensite phase transforms into the austenite phase.

The T_M (149 K) of No.1 is higher than the No.2 (132.5 K) and No.3 (144.8 K), as shown in Table 5. The T_M value is sensitive to the chemical composition and the Mn-excess [38,39]. The Mn-excess atoms increase the e/a, as observed in No. 1, as such the energy of the system increases as the energy of the conduction electrons exceeded the Fermi level and move to the Brillouin zone's corners [3]. The lattice distortion (martensite transition) in these systems accommodates these corner states within a new zone pattern to achieve minimum free energy [40]. Thus, the increase in e/a leads to a higher T_M [3]. The e/a decrease from sample No.1 to No.2 and increases again in case of the No.3, thus, the T_M of No.1 and No.3 is higher than No.2. As shown in Table 5, the T_c increased from 319.2 K to 322.6 K (under the field of 0.01 T) when the HT time increases from one week to three weeks. As shown in Table 4, the Ni content decreases with increasing HT time. The Ni atom has a lower moment than the Mn atom, and substituting the Ni atom for Mn results in the magnetic subsystem's dilution in the austenite phase [27]. Thus, the T_c increased with the decreasing Ni atoms. In addition, residual stress is released and structurally relaxed with longer HT time, which results in an improved T_c [31].

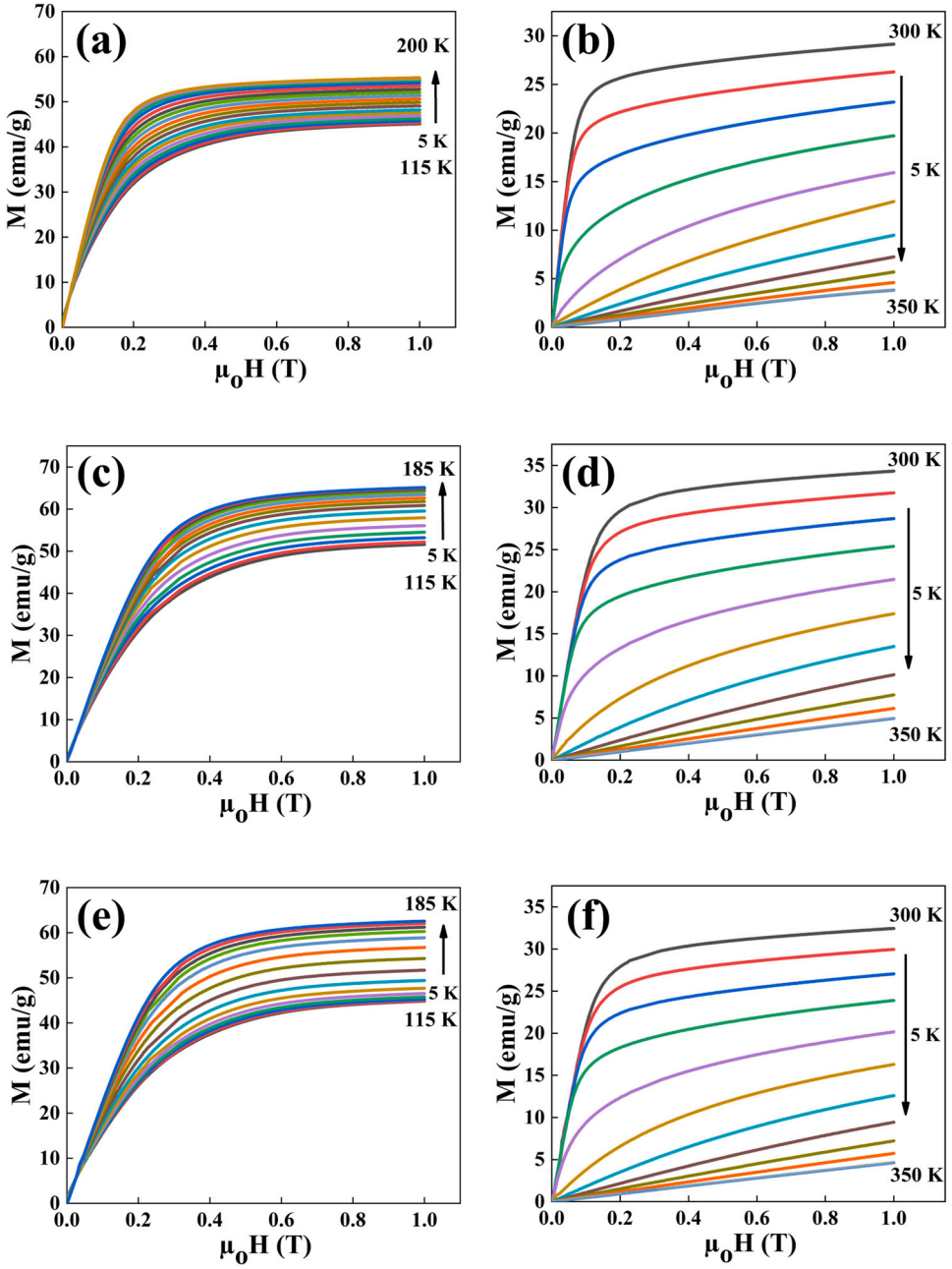

Fig. 10. (a, c, e) Isothermal magnetisation curves of LPBF NiMnSn samples with annealing times of one, two, and three weeks near the T_M; and (b, d, f) Isothermal magnetisation curves of LPBF NiMnSn samples with annealing times of one, two, and three weeks near the T_c.

3.2.3. Isothermal magnetisation

The isothermal magnetisation (M-H) curves were measured around the structural and magnetic transformation temperatures (T_M and T_c) under a decreasing field (1 to 0 T). Fig. 10 shows the isothermal magnetisation M-H curves at different temperatures (every 5 K) around T_M (a, c, and e) and T_c (b, d, and f) of three samples. The field scanning was performed from 1 T to 0 T. From Fig. 10 a, c, and e, the magnetisation increases with increasing temperatures as the weak magnetic martensite gradually transformed into the strong magnetic austenite. Fig. 10 b, d, and f show that the austenite converted from ferromagnetic (FM) to paramagnetic (PM) states at higher temperatures, which led to a decrease in magnetisation.

The Arrott plots were employed to determine the nature of each magnetic transition, as shown in Fig. 11. The negative slope of Arrott plots around T_M and T_c indicates SOPT [41]. However, the existing magnetic hysteresis in the M-T curve (Fig. 9) confirms the FOPT transition around T_M [42]. Fig. 11 a, c, and e reveal the SOPT nature around the T_M due to the weak FOPT around T_M. The suppression/weakness of the FOPT arises from the existing Mn segregation (see Figs. 5 and 6), the NiSn-rich phases within the $L2_1$ phase (see Fig. 6), and the inhomogeneous chemical composition. For NiMnSn alloys with higher Sn content, FOPT is not observed [3,27]. As the SOPT is observed in Arrott plots, the magnetic field dependence of ΔS should vary according to Eq. (6) [43,44]. In Eq. (6), a is a constant and the magnetic state of the sample determines **n** power [43]. The ΔS dependence on the magnetic field (see Equation (7)) confirms the nature of the magnetic transition [45].

$$\Delta S = \mathbf{a}(\mu_0 H)^{\mathbf{n}} \tag{6}$$

Fig. 12 shows the value of the **n** constant is below 2, which is the case of SOPT around both T_c and T_M [46,47].

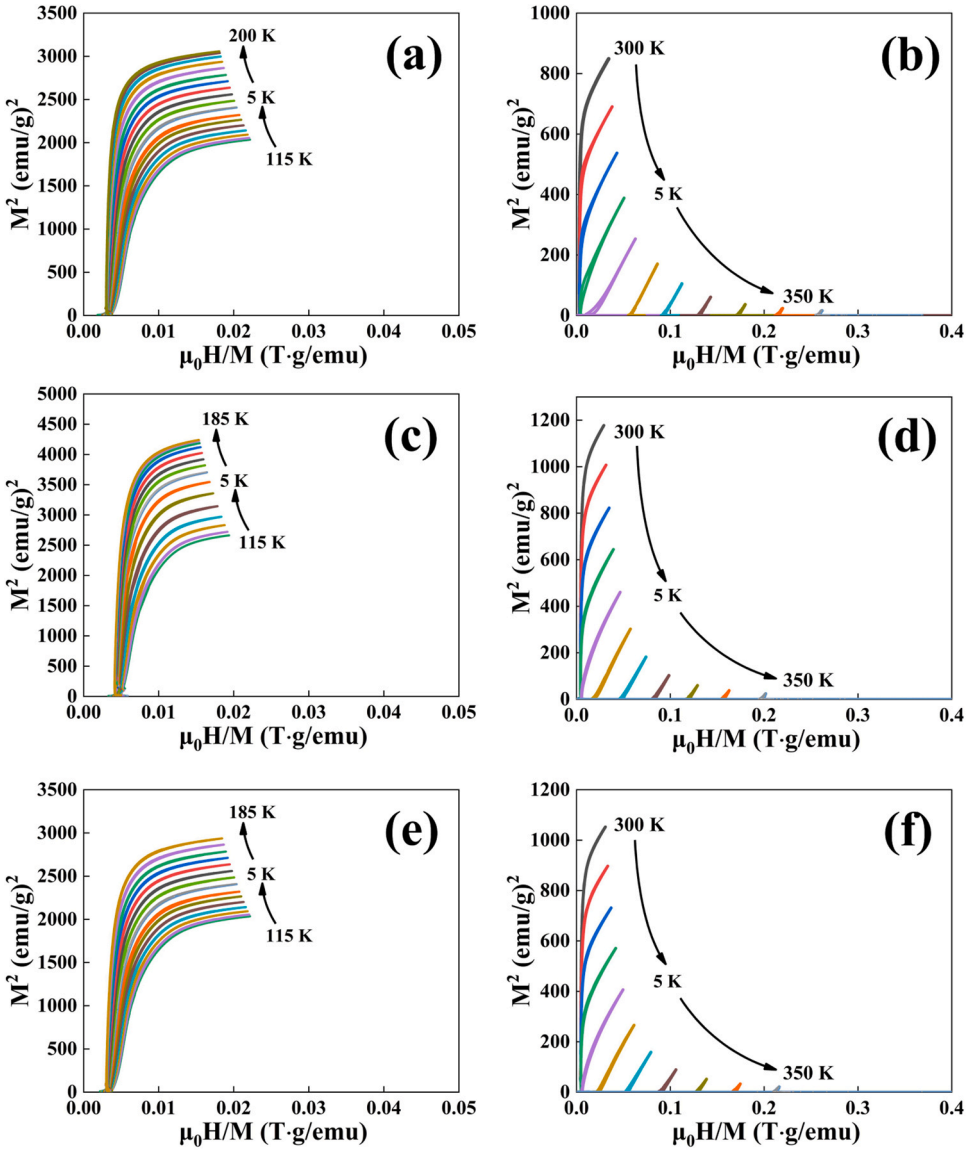

Fig. 11. Arrott plots of annealed LPBF block samples with annealing time of one, two, and three weeks near (a,c,e) the martensitic transformation temperature and (b,d,f) near T_c.

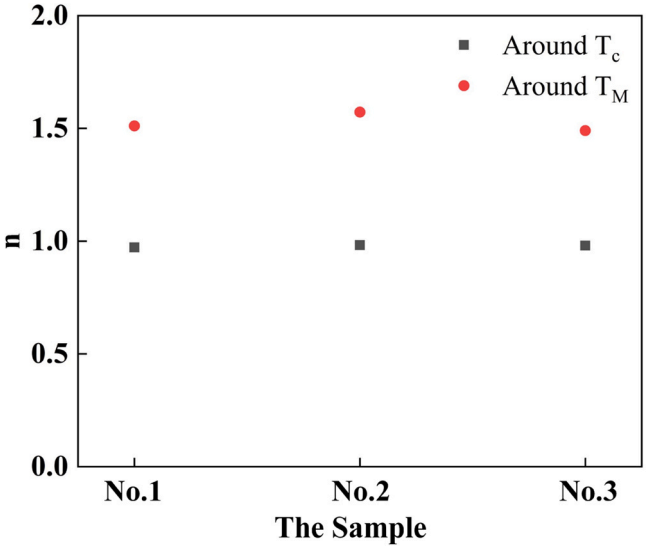

Fig. 12. The value of **n** around the T_c and T_M.

$$\Delta S \alpha H^{n} \quad (7)$$

3.2.4. Magnetocaloric effect (MCE)

Maxwell's relation (Eq. (1)) was applied to calculate the magnetic entropy change under 1 T field near T_c and T_M. As shown in Fig. 13 a, the maximum magnetic entropy change (ΔS_m) values around the martensitic transformation region increased from about 0.2 J kg^{-1} K^{-1} to 0.45 J kg^{-1} K^{-1} when the HT time increased from one week to three. The No.2 and No.3 samples show better MCE than No.1, as the chemical composition is more homogeneous. As shown in Fig. 13 b, the ΔS_m of No.1 sample around T_c (0.90 J kg^{-1}K^{-1} at 315 K) is slightly lower than No.3 (0.94 J kg^{-1}K^{-1} at 320 K) and No.2 (0.99 J kg^{-1}K^{-1} at 320 K).

Thus, the different HT times did not significantly affect the MCE of the LPBF sample. This is expected as the FM order is almost entirely defined by the positive exchange interactions between the Mn and Ni atoms [48], thus, as the chemical composition (Table 4) has minimal change with HT, this will also remain unchanged. Dan et al. also reported this phenomenon [10]. However, the temperature of ΔS_m of No.1 is lower than No.2 and No.3 samples due to different T_c.

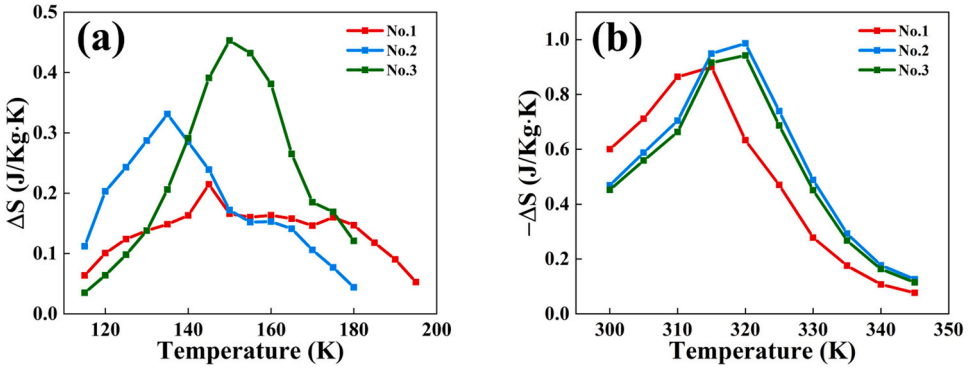

Fig. 13. (a) Thermal variation of ΔS around the T_M of the HT block samples; and (b) thermal variation of ΔS around the T_c of the HT block samples.

4. Conclusion

This study presents a distinct influence of the heat treatment (HT) process on applying Laser Powder Bed Fusion (LPBF) NiMnSn Heusler Alloys for magnetic refrigeration applications. The following conclusions are drawn from this work:

1. All samples exhibited highly ordered cubic $L2_1$ austenite at room temperature. The Mn segregation was ubiquitous even after a three weeks HT process. The Mn segregation contained oxygen elements and was confirmed by XRD, EBSD and TEM results to be MnO.
2. All grains within LPBF samples were equiaxed, and all samples did not possess strong preferential orientations. The two and three weeks HT processes decrease the average local misorientation.
3. The chemical composition was more uniform when increasing the HT time, where composition deviation (ζ) decreased from 0.413 to 0.339 with the increasing HT time. Different chemical compositions resulted in different transition temperatures. The martensite transformation temperature (149 K) of samples HT for one week was higher than samples HT for two weeks (132.5 K) and three weeks (144.8 K), while the Curie temperature (T_c) increased from 319.2 K to 322.6 K with increased HT duration.
4. The maximum magnetic entropy change (ΔS_m) values around T_M increased from about 0.2 J kg^{-1} K^{-1}–0.45 J $kg^{-1}K^{-1}$ when the HT time increased from one week to three. Around T_c the ΔS_m of the one-week HT (0.90 J $kg^{-1}K^{-1}$ at 315 K) was slightly lower than three-week HT (0.94 J kg^{-1} K^{-1} at 320 K) and two-week HT (0.99 J $kg^{-1}K^{-1}$ at 320 K).

CRediT authorship contribution statement

Kun Sun: Writing – original draft, Visualization, Validation, Software, Methodology, Investigation, Formal analysis, Data curation, Conceptualization. **Abd El-Moez A. Mohamed:** Writing – review & editing, Supervision, Methodology, Investigation, Formal analysis, Conceptualization. **Sheng Li:** Writing – review & editing, Methodology. **Kan Ma:** Investigation, Data curation. **Ranxi Duan:** Software. **Oliver Peter Brooks:** Formal analysis. **Minki Jeong:** Investigation. **Jake Head:** Investigation. **Richard S. Sheridan:** Supervision, Methodology. **Moataz M. Attallah:** Supervision, Project administration, Funding acquisition, Conceptualization, Writing – review & editing.

Data Availability

Data will be made available on request.

Declaration of Competing Interest

The authors declare the following financial interests/personal relationships which may be considered as potential competing interests: Kun Sun reports financial support was provided by China Scholarship Council. The authors declared that they have no conflicts of interest to this work.

Acknowledgments

KS would like to thank the China Scholarship Council and the University of Birmingham for co-funding his PhD project. The authors would like to thank the Centre for Electron Microscopy in the University of Birmingham.

References

[1] V. Franco, J.S. Blazquez, B. Ingale, A. Conde, The magnetocaloric effect and magnetic refrigeration near room temperature: materials and models, Annu. Rev. Mater. Res. 42 (2012) 305–342.
[2] A.E.-M.A. Mohamed, M. Jeong, R.S. Sheridan, M.M. Attallah, Enabling high efficiency magnetic refrigeration using laser powder bed fusion of porous LaCe(Fe,Mn,Si)13 structures, Addit. Manuf. 51 (2022) 102620.
[3] A. Cakir, L. Righi, F. Albertini, M. Acet, M. Farle, Intermartensitic transitions and phase stability in Ni50Mn50-xSnx Heusler alloys, Acta Mater. 99 (2015) 140–149.
[4] L. Hou, Y. Dai, Y. Fautrelle, Z. Li, Z. Ren, X. Li, Control of microstructure using magnetic fields and study of the mechanical behavior of Ni-rich Ni-Mn-Ga alloys, Acta Mater. 199 (2020) 383–396.
[5] N.M. Bruno, C. Yegin, I. Karaman, J.H. Chen, J.H. Ross, J. Liu, J.G. Li, The effect of heat treatments on Ni43Mn42Co4Sn11 meta-magnetic shape memory alloys for magnetic refrigeration, Acta Mater. 74 (2014) 66–84.
[6] A.S. Kalbfleisch, G. Matthews, P.J. Jacques, On the influence of the cooling rate on the martensitic transformation of Ni-Mn-Sn Heusler alloys, Scr. Mater. 114 (2016) 121–124.
[7] H.C. Xuan, K.X. Xie, D.H. Wang, Z.D. Han, C.L. Zhang, B.X. Gu, Y.W. Du, Effect of annealing on the martensitic transformation and magnetocaloric effect in Ni44.1Mn44.2Sn11.7 ribbons, Appl. Phys. Lett. 92 (24) (2008) 242506.
[8] M. Nazmunnahar, T. Ryba, J.J. del Val, M. Ipatov, J. González, V. Hašková, P. Szabó, P. Samuely, J. Kravcak, Z. Vargova, R. Varga, Half-metallic Ni2MnSn Heusler alloy prepared by rapid quenching, J. Magn. Magn. Mater. 386 (2015) 98–101.
[9] Martensitic transformation and related magnetic effects in Ni—Mn-based ferromagnetic shape memory alloys, Chinese Phys B 22(7), 2013, 077506.
[10] N.H. Dan, N.H. Duc, N.H. Yen, P.T. Thanh, L.V. Bau, N.M. An, D.T.K. Anh, N.A. Bang, N.T. Mai, P.K. Anh, T.D. Thanh, T.L. Phan, S.C. Yu, Magnetic properties and magnetocaloric effect in Ni-Mn-Sn alloys, J. Magn. Magn. Mater. 374 (2015) 372–375.
[11] A. Ghosh, K. Mandal, Effect of structural disorder on the magnetocaloric properties of Ni-Mn-Sn alloy, Appl. Phys. Lett. 104 (3) (2014).
[12] H.D. Nguyen, T.H. Do, H.Y. Nguyen, T.T. Pham, H.D. Nguyen, T.N.N. Nguyen, D.T. Tran, T.L. Phan, S.C. Yu, Influence of fabrication conditions on giant magnetocaloric effect of Ni–Mn–Sn ribbons, Advances in Natural, Sci.: Nanosci. Nanotechnol. 4 (2) (2013) 025011.
[13] M. Yin, P. Nash, W. Chen, S. Chen, Standard enthalpies of formation of selected Ni2YZ Heusler compounds, J. Alloy Compd. 660 (2016) 258–265.
[14] H. Zhang, X. Zhang, Y. Xiao, M. Yang, Z. Xu, Z. Yao, M. Qian, L. Zhang, L. Yin, D. Jia, Peculiarity of magnetocaloric and magnetoresistance effects in Ni–Mn–Sn–Fe alloy with successive metamagnetic structural transitions, Intermetallics 149 (2022) 107651.

[15] W. Sun, X. Lu, Z. Wei, Q. Li, Z. Li, Y. Zhang, J. Liu, Multicaloric effect in Ni–Mn–Sn metamagnetic shape memory alloys by laser powder bed fusion, Addit. Manuf. 59 (2022) 103125.
[16] R. Duan, S. Li, B. Cai, W. Zhu, F. Ren, M.M. Attallah, A high strength and low modulus metastable β Ti-12Mo-6Zr-2Fe alloy fabricated by laser powder bed fusion in-situ alloying, Addit. Manuf. (2020) 101708.
[17] M. Hasegawa, Chapter 3.3 - Ellingham diagram, in: S. Seetharaman (Ed.), Treatise on Process Metallurgy, Elsevier, Boston, 2014, pp. 507–516.
[18] M.E. Lines, E.D. Jones, Antiferromagnetism in the face-centered cubic lattice. II. Magnetic properties of MnO, Phys. Rev. 139 (4A) (1965) A1313–A1327.
[19] G.H. Lee, S.H. Huh, J.W. Jeong, B.J. Choi, S.H. Kim, H.-C. Ri, Anomalous magnetic properties of MnO nanoclusters, J. Am. Chem. Soc. 124 (41) (2002) 12094–12095.
[20] S.-S. Rui, L.-S. Niu, H.-J. Shi, S. Wei, C.C. Tasan, Diffraction-based misorientation mapping: a continuum mechanics description, J. Mech. Phys. Solids 133 (2019) 103709.
[21] E.M. Fayed, M. Saadati, D. Shahriari, V. Brailovski, M. Jahazi, M. Medraj, Effect of homogenization and solution treatments time on the elevated-temperature mechanical behavior of Inconel 718 fabricated by laser powder bed fusion, Sci. Rep. 11 (1) (2021) 2020.
[22] D. Kong, C. Dong, X. Ni, L. Zhang, J. Yao, C. Man, X. Cheng, K. Xiao, X. Li, Mechanical properties and corrosion behavior of selective laser melted 316L stainless steel after different heat treatment processes, J. Mater. Sci. Technol. 35 (7) (2019) 1499–1507.
[23] A. Tajyar, N. Brooks, N. Holtham, R. Rowe, D.J. Newell, A.N. Palazotto, K. Davami, Effects of a modified heat-treatment on microstructure and mechanical properties of additively manufactured Inconel 718, Mater. Sci. Eng. A 838 (2022) 142770.
[24] P. Lehto, Adaptive domain misorientation approach for the EBSD measurement of deformation induced dislocation sub-structures, Ultramicroscopy 222 (2021) 113203.
[25] R. Unnikrishnan, S.M. Northover, H. Jazaeri, P.J. Bouchard, Investigating plastic deformation around a reheat-crack in a 316H austenitic stainless steel weldment by misorientation mapping, Procedia Struct. Integr. 2 (2016) 3501–3507.
[26] T.-S. Jun, A.M. Korsunsky, Evaluation of residual stresses and strains using the Eigenstrain reconstruction method, Int. J. Solids Struct. 47 (13) (2010) 1678–1686.
[27] M.K. Ray, K. Bagani, S. Banerjee, Effect of excess Ni on martensitic transition, exchange bias and inverse magnetocaloric effect in Ni2+xMn1.4-xSn0.6 alloy, J. Alloy Compd. 600 (2014) 55–59.
[28] P. Czaja, A. Wierzbicka-Miernik, Ł. Rogal, Segregation and microstructure evolution in chill cast and directionally solidified Ni-Mn-Sn metamagnetic shape memory alloys, J. Cryst. Growth 492 (2018) 50–59.
[29] Y. Zhang, L.L. Zhang, Q. Zheng, X.Q. Zheng, M. Li, J. Du, A. Yan, Enhanced magnetic refrigeration properties in Mn-rich Ni-Mn-Sn ribbons by optimal annealing, Sci. Rep. 5 (2015).
[30] T. Chabri, A. Venimadhav, T.K. Nath, Interplay of austenite and martensite phase inside martensite transition regime and its role on magnetocaloric effect and magnetoresistance in Ni-Mn-Sn based Heusler alloy, Intermetallics 102 (2018) 65–71.
[31] H. Zhang, X. Zhang, M. Qian, L. Zhang, L. Zhang, S. Chai, L. Yin, Martensite transformation behavior and magnetocaloric effect in annealed Ni-Co-Mn-Sn microwires, Mater. Sci. Eng. B 274 (2021) 115477.
[32] Z. Li, S. Dong, Z. Li, B. Yang, F. Liu, C.F. Sánchez-Valdés, J.L. Sánchez Llamazares, Y. Zhang, C. Esling, X. Zhao, L. Zuo, Giant low-field magnetocaloric effect in Si alloyed Ni-Co-Mn-In alloys, Scr. Mater. 159 (2019) 113–118.
[33] X. Sun, E. Feng, Y. Su, K. Nemkovski, O. Petracic, T. Brückel, Magnetic properties and spin structure of MnO single crystal and powder, J. Phys.: Conf. Ser. 862 (1) (2017) 012027.
[34] A.S.B. Madiligama, P. Ari-Gur, Y. Ren, V.V. Koledov, E.T. Dilmieva, A.P. Kamantsev, A.V. Mashirov, V.G. Shavrov, L. Gonzalez-Legarreta, B.H. Grande, Thermal and magnetic hysteresis associated with martensitic and magnetic phase transformations in Ni52Mn25In16Co7 Heusler alloy, J. Magn. Magn. Mater. 442 (2017) 25–35.
[35] B. Hernando, J.L.S. Llamazares, J.D. Santos, M.L. Sánchez, L. Escoda, J.J. Suñol, R. Varga, C. García, J. González, Grain oriented NiMnSn and NiMnIn Heusler alloys ribbons produced by melt spinning: martensitic transformation and magnetic properties, J. Magn. Magn. Mater. 321 (7) (2009) 763–768.
[36] J. Kamarád, J. Kaštil, M. Friák, M. Mazalová, O. Schneeweiss, M. Míšek, O. Kaman, Z. Arnold, Pressure study of magnetism in off-stoichiometric Ni2MnSn-based alloys, J. Magn. Magn. Mater. 539 (2021) 168345.
[37] K. Sun, A.E.-M.A. Mohamed, S. Li, M. Jeong, J. Head, M.M. Attallah, Laser powder bed fusion of the Ni-Mn-Sn Heusler alloy for magnetic refrigeration applications, Addit. Manuf. 69 (2023) 103536.
[38] V. Chernenko, E. Cesari, V. Kokorin, I. Vitenko, The development of new ferromagnetic shape memory alloys in Ni-Mn-Ga system, Scr. Metall. Et. Mater. 33 (8) (1995) 1239–1244.
[39] P. Entel, M. Siewert, M.E. Gruner, H.C. Herper, D. Comtesse, R. Arróyave, N. Singh, A. Talapatra, V.V. Sokolovskiy, V.D. Buchelnikov, F. Albertini, L. Righi, V.A. Chernenko, Complex magnetic ordering as a driving mechanism of multifunctional properties of Heusler alloys from first principles, Eur. Phys. J. B 86 (2) (2013) 65.
[40] V.A. Chernenko, Compositional instability of β-phase in Ni-Mn-Ga alloys, Scr. Mater. 40 (5) (1999) 523–527.
[41] B.J.Pl Banerjee, On a generalised approach to first and second order magnetic transitions, 12(1) (1964) 16–17.
[42] K. Liu, S. Ma, C. Ma, X. Han, K. Yu, S. Yang, Z. Zhang, Y. Song, X. Luo, C. Chen, S.U. Rehman, Z. Zhong, Martensitic transformation and giant magneto-functional properties in all-d-metal Ni-Co-Mn-Ti alloy ribbons, J. Alloy Compd. 790 (2019) 78–92.
[43] A.E.-M.A. Mohamed, V. Vega, M. Ipatov, A.M. Ahmed, B. Hernando, Annealing temperature effect on magnetic and magnetocaloric properties of manganites, J. Alloy Compd. 665 (2016) 394–403.
[44] V.K. Pecharsky, K.A. Gschneidner Jr, Magnetocaloric effect from indirect measurements: Magnetisation and heat capacity, J. Appl. Phys. 86 (1) (1999) 565–575.
[45] T.D. Shen, R.B. Schwarz, J.Y. Coulter, J.D. Thompson, Magnetocaloric effect in bulk amorphous Pd40Ni22.5Fe17.5P20 alloy, J. Appl. Phys. 91 (8) (2002) 5240–5245.
[46] J.Y. Law, V. Franco, L.M. Moreno-Ramírez, A. Conde, D.Y. Karpenkov, I. Radulov, K.P. Skokov, O. Gutfleisch, A quantitative criterion for determining the order of magnetic phase transitions using the magnetocaloric effect, Nat. Commun. 9 (1) (2018) 2680.
[47] F. Chen, J.L. Sánchez Llamazares, C.F. Sánchez-Valdés, Fenghua Chen, Zongbin Li, Y.X. Tong, L. Li. Large magnetic entropy change and refrigeration capacity around room temperature in quinary $Ni_{41}Co_{9-x}Fe_xMn_{40}Sn_{10}$ alloys (x= 2.0 and 2.5). Journal of Alloys and Compounds 825, 2020 https://www.sciencedirect.com/science/article/pii/S0925838820304163.
[48] S. Singh, L. Caron, S.W. D'Souza, T. Fichtner, G. Porcari, S. Fabbrici, C. Shekhar, S. Chadov, M. Solzi, C. Felser, Large magnetisation and reversible magnetocaloric effect at the second-order magnetic transition in heusler materials, Adv. Mater. 28 (17) (2016) 3321–3325.